RESEARCH ARTICLE | JULY 07 2023

Enhanced confinement induced by pellet injection in the stellarator TJ-II

I. García-Cortés ; K. J. McCarthy ; T. Estrada ; V. Tribaldos ; D. Medina-Roque ; B. van Milligen ; E. Ascasíbar ; R. Carrasco ; A. A. Chmyga; R. García ; J. Hernández-Sánchez ; C. Hidalgo ; A. S. Kozachek; F. Medina ; M. A. Ochando ; J. L. de Pablos ; N. Panadero ; I. Pastor

Phys. Plasmas 30, 072506 (2023)
https://doi.org/10.1063/5.0151395

Enhanced confinement induced by pellet injection in the stellarator TJ-II

Cite as: Phys. Plasmas **30**, 072506 (2023); doi: 10.1063/5.0151395
Submitted: 21 March 2023 · Accepted: 17 June 2023 ·
Published Online: 7 July 2023 · Corrected: 30 August 2023

I. García-Cortés,[1,a)] K. J. McCarthy,[1] T. Estrada,[1] V. Tribaldos,[2] D. Medina-Roque,[1] B. van Milligen,[1] E. Ascasíbar,[1] R. Carrasco,[1] A. A. Chmyga,[3] R. García,[1] J. Hernández-Sánchez,[1] C. Hidalgo,[1] A. S. Kozachek,[3] F. Medina,[1] M. A. Ochando,[1] J. L. de Pablos,[1] N. Panadero,[1] and I. Pastor[1]

AFFILIATIONS

[1]Laboratorio Nacional de Fusión, Centro de Investigaciones Energéticas Medioambientales y Tecnológicas, Madrid 28040, Spain
[2]Departamento de Física, Universidad Carlos III de Madrid, Leganés, Madrid 28911, Spain
[3]Institute of Plasma Physics, National Science Center Kharkov Institute of Physics and Technology, Kharkov 61108, Ukraine

[a)]**Author to whom correspondence should be addressed:** isabel.garciacortes@ciemat.es

ABSTRACT

Enhanced confinement is observed in neutral beam injector (NBI)-heated hydrogen discharges made in the stellarator TJ-II after the injection of a single cryogenic fuel pellet into the plasma core. In addition to the expected increase in electron density, n_e, in the core after pellet injection (PI), the plasma diamagnetic energy content is seen to rise, with respect to similar discharges without PI, by up to 40%. Furthermore, the energy confinement time, τ^{E}_{diag}, as determined using a diamagnetic loop, is enhanced when compared to predictions obtained using the International Stellarator Scaling law [H. Yamada *et al.*, Nucl. Fusion **45**, 1684 (2005)] and the triple product, $n_e \cdot T_i \cdot \tau^{E}_{diag}$, exhibits a clear bifurcation point toward an improved confinement branch as compared to the branch product predicted by this scaling law. In general, once such a pellet-induced enhanced confinement (PiEC) phase has been established, it is characterized by steepened radial density gradients, by more negative plasma potential in the core, more negative radial electric fields, E_r, across a broad plasma region, as well as by reductions in density and plasma potential fluctuations in the density gradient region. In addition, experimental observations show increased peaking of core radiation losses, this pointing to edge/core plasma decoupling. In parallel, neoclassical simulations of reference and PiEC plasmas predict increased particle and energy confinement times during a PiEC phase together with a more negative E_r profile. Qualitative rather than quantitative agreement with experimental parameters is found, indicating that turbulence seems to play a significant role here. In summary, single cryogenic pellet injection facilitates the achievement of an enhanced operational regime that was previously not observed in NBI-heated discharges of the TJ-II.

I. INTRODUCTION

Pellet injection (PI) is widely used in magnetic confinement fusion (MCF) devices to achieve deep and efficient core plasma fueling, this being essential for future fusion reactors.[1,2] Indeed, improved plasma performance, associated with core fueling with pellets, has been described for numerous MCF devices.[3–7] A common characteristic of post-injection plasma is a clear increase in energy confinement when compared to similar discharges fueled by gas puff and/or recycling only. In some cases, pellets have been considered as the trigger for an L–H transition, for instance, in the tokamaks TUMAN-3M and MAST.[8,9] In other devices, it has been reported that PI extends plasma performance via the development of internal transport barriers that give rise to efficient fueling with no significant measurable impact on the edge density profile, e.g., in ASDEX-U.[4] In this work, attention is turned toward stellarators, e.g., W7-X,[3] LHD,[5,6] Heliotron J,[7] and, in particular, the medium-sized heliac TJ-II.[10]

In the case of LHD, the operational region of neutral beam injector (NBI)-heated plasma was first extended to conditions well beyond those obtainable by gas fueling using pellet injection while in parallel, achieving and maintaining a favorable dependence of energy confinement on density.[6] It was noted therein that no obvious density-related confinement degradation occurred beyond the predicted density limit,[11] unlike in the case of gas puffing where a confinement degradation was observed at lower densities. A more recent experiment with single pellet injection into NBI-heated plasma addressed the important question of post-injection transport fueling the plasma core.[12] It was

reported therein that the mean density increased sharply after PI and became relatively stationary after about 1 s. In parallel, the central density exhibited two different time scale responses, one involving a 20% increase in central density after a few 10s of milliseconds, the other involving a recovery of temperature and a further increase in central density on a time scale of several 100s of milliseconds followed by a decrease in central density. In parallel, the stored plasma energy showed a fast increase followed by a more moderate decrease, this being consistent with density and temperature evolutions. Then, it was concluded that particle transport from peripheral pellet deposition was effective in fueling the plasma core on the time scale of central density relaxation. It was also noted that while a response was observed in the radial electric field, the change in sign predicted by local neoclassical (NC) theory did not occur. Finally, in another study, multi-pellet injection was used to create an internal diffusion barrier (IDB) that results in an increase in core density and large radial density gradients. (Ref. 13 and references therein.) Once developed, this IDB structure is maintained long after PI, thereby extending its improved confinement regime.

Next, in Heliotron E, in addition to increased core density, a more negative radial electric field, E_r, was found across a radial region that extended from the near-edge region to the bulk plasma.[14] However, the origins of such improvements were not investigated further. More recently, after single PI into neutral beam injector (NBI)-only heated plasma of Heliotron J, strongly peaked density profiles were observed and, as a result, higher stored energies were achieved when compared with values achieved with gas puffing only.[7] It was noted by the authors that the edge-region density remained close to pre-injection levels and that a steep density gradient (5–6 times higher than before PI) was formed in the plasma core. They considered that the observed plasma characteristics resembled superdense core IDB plasmas achieved in the LHD.

Finally, in the case of the stellarator W7-X, large transient improvements in energy confinement were reported for some pellet-fueled experiments performed with its standard magnetic configuration in which the plasma was heated using electron cyclotron resonance heating (ECRH) only.[15,16] In one experiment, a train of hydrogen pellets was injected at a frequency of 30 Hz into plasma heated with ~1.6 MW of ECRH, this initiating a density ramp that led to a central density of the order 10^{20} m^{-3}. Then, just before injections were terminated, the ECRH power was increased by a factor three and, soon after, the density decayed, the central electron and ion temperatures recovered and rose to >3 keV, and the stored diamagnetic energy, as measured by a diamagnetic loop, rose to a maximum value of about 1.1 MJ, this being maintained for several hundreds of milliseconds. It was summarized that the plasma parameters achieved during such a post-injection phase were significantly higher than those achieved for comparable gas-fueled discharges, that the enhanced plasma parameters corresponded to a record triple product value for W7-X, and that the energy confinement time exceeded the empirical stellarator scaling ISS04 value by about 30%. It was argued that the improvements in heat transport could be related to the peaked post-injection density profiles that led to a stabilization of the ion-scale turbulence. In a parallel paper, a strong negative E_r was reported during the post-pellet enhanced confinement phase,[3,17] this being mainly reproduced by neoclassical simulations. Concurrently, a reduction in density fluctuation levels occurred, with plasma profile evolution after PI and the stabilization effect of the E_r profile being identified as the dominant players in the stabilization of the plasma turbulence.

In the stellarator TJ-II, pellet studies have focused to date on the physics of pellet ablation and plasmoid drift,[18,19] pellet fueling efficiency,[10,20] pellet-induced magnetic activity,[21] and simulations of pellet particle transport after PI into plasma with a hollow-density profile.[22] In this paper, we investigate how the injection of a single fuel pellet into NBI-heated plasma affects global plasma confinement. For instance, we compare the improved energy confinement observed after PI with energy confinement in reference plasmas having similar operational conditions and with predictions obtained using the International Stellarator Scaling law, ISS04.[23] In addition, neoclassical (NC) and transport code simulations are performed to obtain particle and energy confinement times, as well as E_r, with and without PI in representative NBI-heated plasmas in TJ-II. Finally, we compare code outputs, where possible, with experimental values and discuss our findings.

II. EXPERIMENTAL ARRANGEMENT

The TJ-II is four-period heliac-type stellarator with major radius, $R, = 1.5$ m, average minor radius, $a, \leq 0.22$ m, plasma volume contained within the last-closed magnetic surface, $V_{plasma}, \leq 1.1$ m^3, and on-axis magnetic field, $B_0, \leq 1.1$ T.[24] Plasmas are created using microwave heating generated by two gyrotrons operated at 53.2 GHz, the second harmonic of its electron cyclotron resonance frequency (total $P_{ECRH} \leq 500$ kW). With these, plasma can be maintained for up to 300 ms and central electron densities, n_{e0}, and temperatures, T_{e0}, up to 1.7×10^{19} m^{-3} and 1.5 keV, respectively, are achieved, albeit not simultaneously. The corresponding central ion temperature, T_{i0}, is ≤80 eV. Additional heating is provided by two tangential NBI systems operated in a counter/co-counter configuration (anti-parallel and/or parallel to the toroidal magnetic field direction)[25] (see Fig. 1). With these, up to ~1 MW of total additional power can be injected through the NBI port holes into the vacuum chamber for ≤120 ms and n_{e0}, T_{e0}, and T_{i0} up to 8×10^{19} m^{-3}, 400, and 120 eV, respectively, can be achieved with a boron plus lithium coating on the inner vessel wall.[26]

For this work, a four-pellet pipe-gun type injector system has been operated.[27] Although four pellet sizes are available, only 0.66- or 0.76-mm-diameter pellets are employed here. Straight guide tubes direct pellets (1 of either diameter per discharge) along a flight path toward the magnetic axis, these entering the plasma from its outer edge. Pellet masses and velocities are determined using light-gate and microwave cavity diagnostics positioned along these guide tubes. Pellet ablation is followed using fiber-optic cables fitted with narrowband interference filters (centered at 660 ± 2 nm) that are positioned on the airside of viewports located in the same machine sector and connected to light-sensitive silicon diode detectors.

TJ-II is equipped with a large range of diagnostics.[28] Figure 1 shows the distribution around TJ-II of the main diagnostics of interest. These include a Thomson scattering (TS) system that provides one set of n_e and T_e profiles ($0 \leq \rho \leq$ ~0.8, where $\rho = r/a$ is normalized plasma radius and r is plasma minor radius) per discharge with high spatial resolution;[29] a microwave interferometer that provides a time trace of line-averaged electron density, $\langle n_e \rangle(t)$, Mirnov coils, a diamagnetic loop that allows measurement of stored diamagnetic energy, W^E_{diag};[30] light-sensitive monitors that follow plasma Balmer Hα

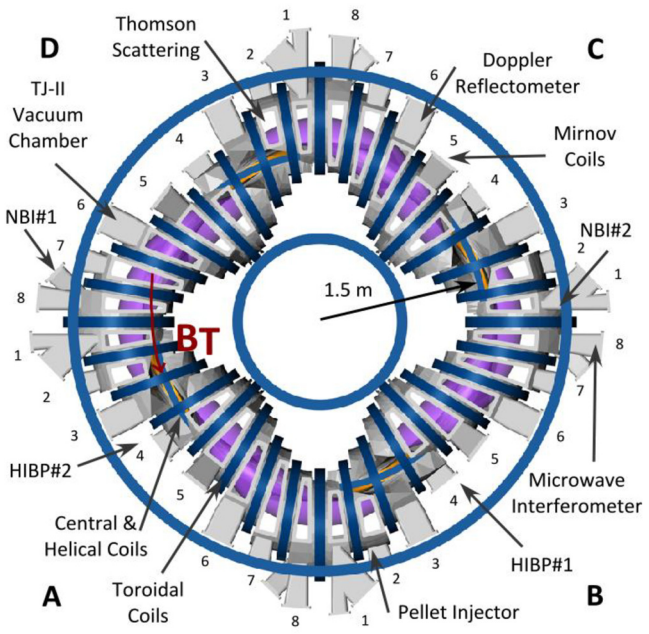

FIG. 1. lhs: Bird's-eye view sketch of the stellarator TJ-II. The locations of cited diagnostics as well as of quadrants A through to D, plus sectors 1 to 8 of each quadrant, are indicated. The vacuum chamber is shown in gray, magnetic field generation coils are shown in the dark blue (vertical, toroidal, and central) and orange (helical), and the plasma is shown in purple. The toroidal magnetic field direction is anti-clockwise.

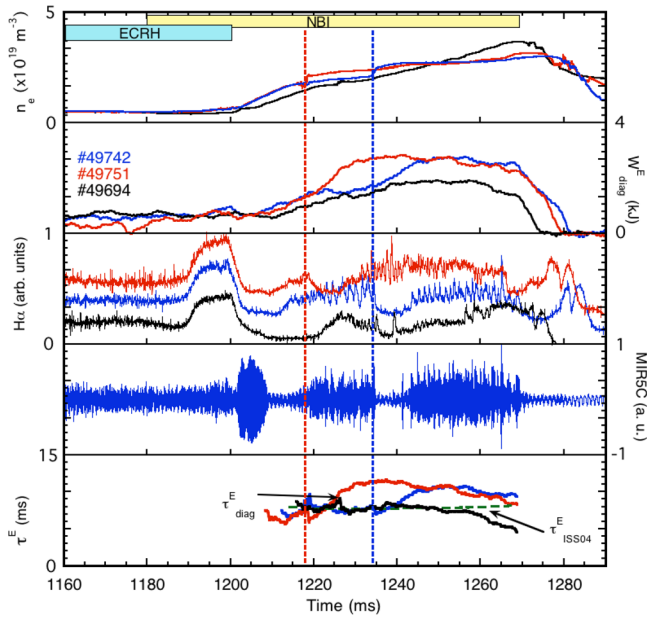

FIG. 3. Time traces of selected plasma parameters along TJ-II discharges 49694 (black), 49742 (navy), and 49751 (red). 220 kW of ECR heating is provided from 1060 to 1200 ms, while 440 kW is injected by NBI#1 between 1180 and 1268 ms. A pellet containing 2.2×10^{19} H atoms is injected at 1234.1 ms of 49742 and at 1218.4 ms of 49751. No pellet is injected into 49694. The plasma parameters shown are, from the top downwards, line-averaged electron density ($\times 10^{19}$ m^{-3}), stored plasma diamagnetic energy, W^{E}_{diag} (kJ), Balmer Hα emission in sector D4 (arb. units), magnetic activity picked up by a Mirnov coil in sector C5 (arb. units), and energy confinement time (ms) estimated using W^{E}_{diag} and absorbed NBI power, τ^{E}_{diag} and τ^{E}_{ISS04} (green dash). Hα traces are offset vertically from each other to aid viewing.

(656.3 nm) emissions, a soft x-ray system;[31] a multi-channel bolometer system that provides plasma emissivity profiles;[32] and a multi-foil soft x-ray detector system that yields measurements of central electron temperature, T_{e0}, along the NBI-heated phase of discharges.[33] In addition, a two-channel Doppler reflectometer and a dual heavy ion beam probe (HIBP) system are also available.[34,35] The two-channel Doppler system is a dual-frequency hopping system (33–50 GHz, X-mode) with a probing beam angle range of $\pm 20°$. It provides measurements of E_r and turbulence dynamics at two selectable radial positions in the outer plasma region. On the other hand, the HIBPs, called HIBP#1

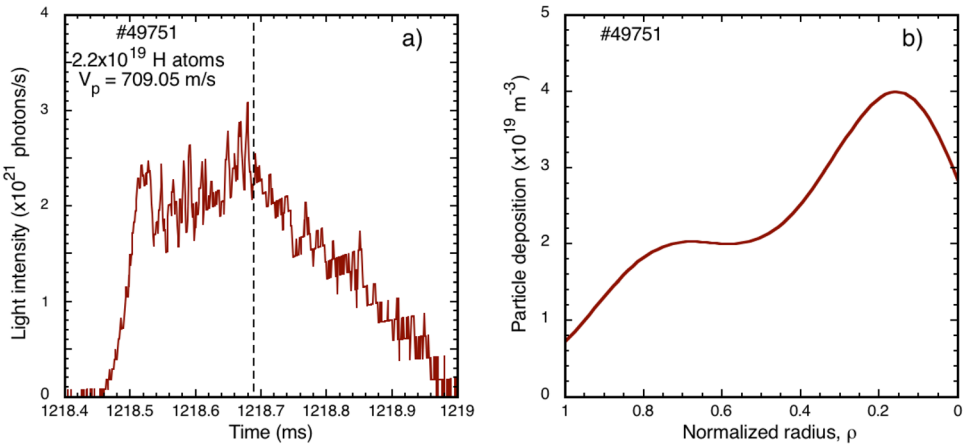

FIG. 2. (a) Plot of the collected Balmer Hα light, emitted during pellet ablation, vs time along discharge 49751. The pellet, with 2.2×10^{19} H atoms, was injected at 709 m/s into the NBI-heated phase of this discharge. It entered the plasma at 1218.406 ms, crossed the magnetic axis at 1218.69 ms (highlighted by vertical dashed line), and was fully ablated before reaching the inner plasma edge. (b) Pellet particle deposition profile, predicted by the TJ-II version of the HPI2 code for the pellet in (a), as a function of normalized plasma radius.[19] This code does not include particle transport after homogenization is completed, i.e., beyond ~1 ms after pellet arrival.

and HIPB#2, provide direct measurements of plasma potential, $\varphi(\rho)$.[36] In addition, they furnish measurements of fluctuations in plasma potential and density, $\tilde{n}_e(t)$, the latter being proportional to fluctuations in the output beam current, $\tilde{I}_{HIBP}$.[37] Finally, with this dual setup, one HIBP can be set to monitor at a fixed radial position ρ, with temporal resolution = 1 μs, while the other can be set to scan between the inner and outer plasma edges, typically once every 10–20 ms.

III. EXPERIMENTAL RESULTS

In the experiments considered here, hydrogen pellets are injected into the NBI-heated phase of TJ-II discharges that are confined using magnetic configurations 100_40_63 ($a = 0.188$ m, $B_0 = 0.95$ T, $\iota_0/2\pi = 1.51$, $V_{plasma} = 1.043$ m^3), 100_44_64 ($a = 0.192$ m, $B_0 = 0.95$ T, $\iota_0/2\pi = 1.56$, $V_{plasma} = 1.1$ m^3), and 100_48_65 ($a = 0.191$ m, $B_0 = 0.95$ T, $\iota_0/2\pi = 1.59$, $V_{plasma} = 1.09$ m^3), where $\iota_0/2\pi$ is the on-axis rotational transform. The configuration label "xxx_yy_zz" represents currents in the circular, helical, and vertical field coils of this current-free stellarator. Plasmas, with hydrogen as the working gas, are created using electron cyclotron resonance heating (ECRH) and once developed additional heating, provided by one or both NBIs, is injected. Now, with regard to PIs, a pellet injected into ECRH plasma is typically fully ablated before reaching the plasma center ($\rho = 0$). The result is a transient increase in plasma line-averaged density, $\langle n_e \rangle$, and a post-injection pellet particle deposition profile that is rather flat with no significant changes in plasma performance.[10] In contrast, the pellet ablation rate is significantly lower for NBI-heated plasma due to reduced T_e; thus, pellets can penetrate beyond the magnetic axis (see Fig. 2(a)). However, because of strong radial drifting of ablated material in TJ-II, post-ablation pellet particle deposition tends to occur in the plasma core for deep pellet penetration (NBI-heated plasmas) and close to the outer edge for shallow penetration (ECRH plasmas).[10,18,19] See Fig. 2(b) where the estimated particle deposition profile for the pellet in Fig. 2(a) is shown. This profile is calculated using the TJ-II version of the HPI2 code.[19] It should be noted that this code does not include particle transport after homogenization is completed, i.e., beyond ~1 ms after pellet arrival. Finally, for both heating scenarios, pellet ablation results in a strong reduction in T_e across the full minor radius and a significant increase in n_e. In the case of NBI-heated plasma, T_e recovery to pre-injection values requires a few milliseconds. In contrast, this recovery time is significantly longer for ECRH plasma.[10]

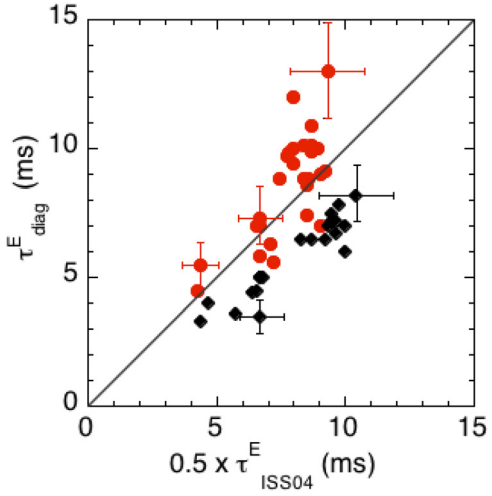

FIG. 4. Confinement times for assessed TJ-II discharges, τ^E_{diag}, vs predicted ISS04 times, τ^E_{ISS04}, with a re-scaling factor of 0.5 as in Refs. 41 and 23. Here, τs are estimated when W^E_{diag} is maximum along each discharge. Data are for NBI-heated plasmas in TJ-II with (red spots) and without (black diamonds) pellet injection (data are for discharges 49690 to 49755, 51040 to 51050, and 52549 to 52562). Error bars are shown for selected data points.

A. Pellet-induced enhanced confinement

As an example, selected plasma parameters are shown for a series of reproducible TJ-II discharges with and without PI, these discharges having a target n_e of ~2.2×10^{19} m^{-3} (see Fig. 3). In the figure, plasma is created in the 100_44_64 configuration using 220 kW of ECRH power, which is switched-off at 1200 ms. Prior to ECRH switch-off, 440 kW of port-through NBI power is switched on at 1180 ms and is injected in the co-counter direction (parallel to the toroidal magnetic field direction, B_T, of Fig. 1). This is maintained until ~1270 ms. A single pellet, containing ~2.2×10^{19} H atoms, is injected into the NBI-heated phase at different times of two of the selected discharges, 49742 and 49751. Signals for a similar discharge, 49694, with no PI and fueled by gas puff and/or wall recycling, are shown for comparison. In the first case, discharge 49751, the pellet crosses the plasma edge at 1218.4 ms and is fully ablated within ~500 μs (see Fig. 2). In the discharges, PI causes an abrupt increase in $\langle n_e \rangle$ together with simultaneous reductions in central ion and electron

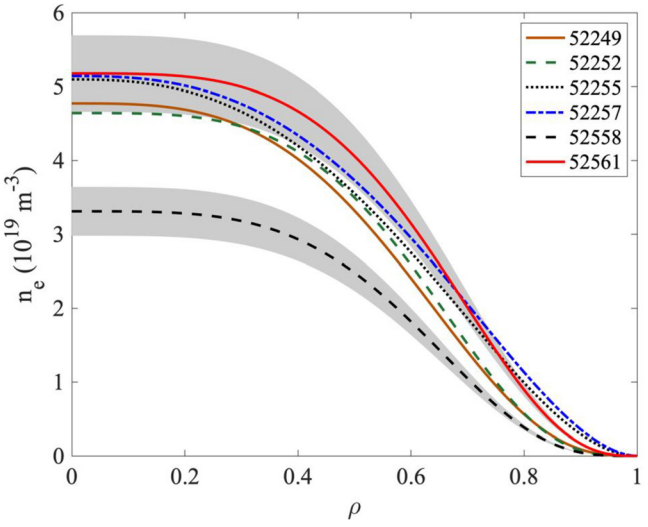

FIG. 5. Evolution of the plasma density profile, obtained using the shot-by-shot method, before and after injection of a single pellet with 1.2 (±0.05) × 10^{19} H atoms into discharges created with the magnetic configuration 100-44-64 and heated by NBI#1, which provides 400 kW of port-through power. Plotted profiles are 52558 (0 ms, dot–dot, black), 52549 (+6 ms after PI, brown, dot–dash), 52552 (+6 ms after PI, brown, dot–dot–dash–dash), 52555 (+16 ms after PI, green, dash–dash), 52557(+21 ms after PI, navy, long dash–short dash), and 52561 (+31 ms after PI, red, continuous). TS data points are not shown for clarity. Shaded zones show the uncertainty band for selected profiles.

temperatures (T_{i0}, T_{e0}), where these decreases are followed by a rapid recovery, i.e., within several milliseconds. Moreover, post-injection reductions in the Hα signal level, Hα fluctuations, and magnetic fluctuations (≲300 kHz) are also observed, see Fig. 3, the latter being associated in TJ-II with a rapid decrease in T_e as observed by a multi-foil x-ray detector.[21,33] Next, as $\langle n_e \rangle$ remains high and T_{i0} plus T_{e0} recover after PI, the plasma diamagnetic energy content, W^E_{diag}, is seen to increase to values that are significantly higher than those achieved in the reference discharge, 49694. Indeed, in the examples explored here, W^E_{diag} increases by ∼40% with respect to the reference discharge, while the energy confinement time, τ^E_{diag}, lengthens from ∼7.6 to ∼11 ms (see Fig. 3). Here, τ^E_{diag} is estimated as $\tau^E_{diag} = W^E_{diag}/(P_{abs} - dW^E_{diag}/dt)$, where absorbed NBI power, P_{abs}, is evaluated using the FAFNER2 code.[38,39] This code estimates absorbed power by considering shine-through, fast-ion, and charge exchange losses. It was benchmarked for TJ-II using plasma profiles from NBI-heated discharges during experimental campaigns.[39] For instance, shine-through losses can be determined using the infrared sensitive imaging cameras that view both graphite beam stops.[40] Through such analysis and experiments, it has been determined that average deviations between calculations for individual discharges, based on experimental density and temperature profiles, and values predicted by FAFNER2 fits are of the order 10%–15%.[39]

In Fig. 3, both W^E_{diag} and τ^E_{diag} remain at the higher levels until NBI switch-off. It is considered that such sustained increases in W^E_{diag} and τ^E_{diag} indicate that these TJ-II plasmas enter an enhanced confinement phase after PI, i.e., a pellet-induced enhanced confinement (PiEC) phase, which persists until NBI switch-off. In order to evaluate such a PiEC phase, post-injection τ^E_{diag} values at maximum W^E_{diag} for the discharges of Fig. 3, as well as for a number of selected NBI-heated discharges exhibiting a PiEC phase, are compared in Fig. 4 with confinement times predicted using the International Stellarator Scaling law, τ^E_{ISS04}.[23] A re-scaling factor of 0.5 is used here for TJ-II.[41] The discharges considered here have post-injection $\langle n_e \rangle$'s from 2.5 × 10^{19} to

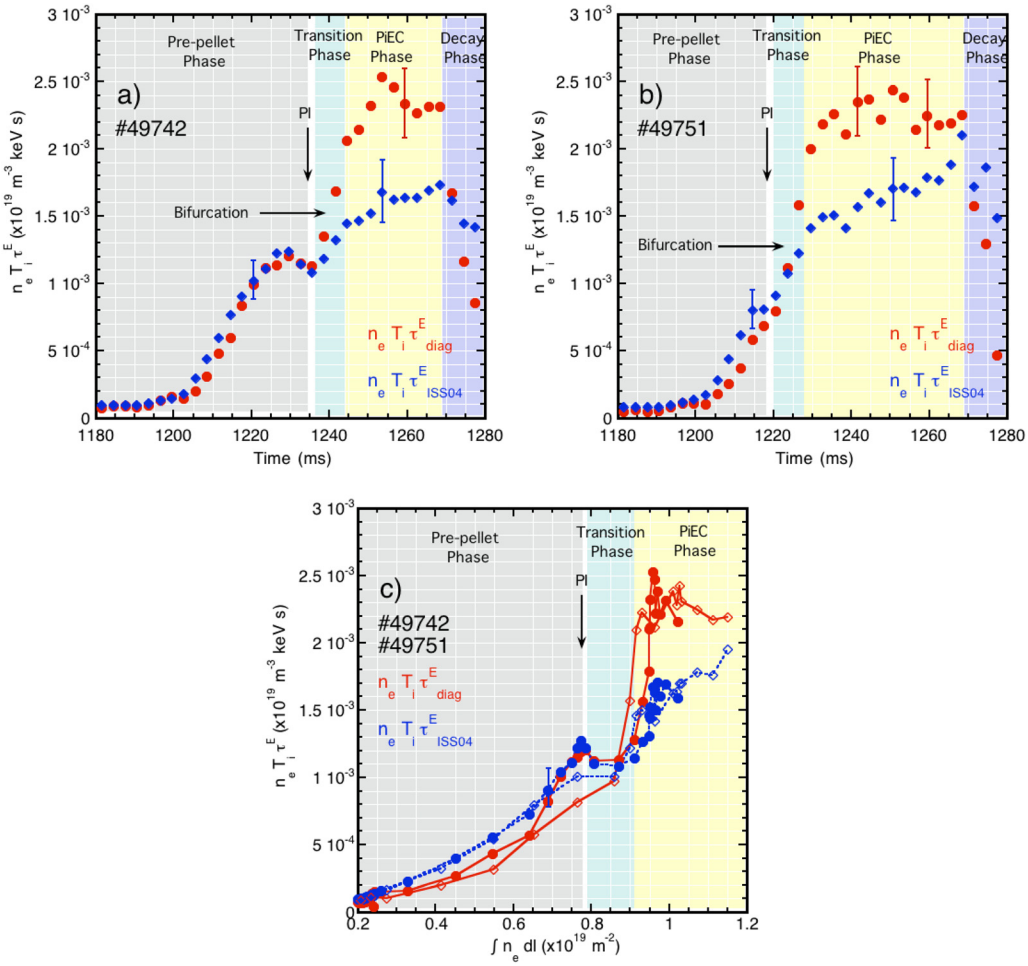

FIG. 6. (a) and (b) Plasma triple product ($n_e \cdot T_i \cdot \tau^E$) vs time along the NBI-heated phase of two TJ-II discharges from the same series as Fig. 3. NBI heating is switched off at 1270 ms. Plasma triple products are compared for τ^E_{diag} and τ^E_{ISS04}. Pellet injections and bifurcation points are indicated by vertical and horizontal arrows, respectively. The pre-pellet, PI, transition, PiEC, and decay phases are highlighted by shading. (c) Plasma triple product vs integrated line-averaged density. Here, • represents data from 49742, while ⌑ represents 49751. Selected error bars are included.

3.5×10^{19} m^{-3}, $\iota_0/2\pi$ from 1.51 to 1.59, and absorbed NBI power between 300 and 600 kW. These are from experiments 39069 to 39073, 43842 to 43874, 49690 to 49754, and 52549 to 52701. It should be noted also that variations in absorbed NBI power and post-injection plasma density give rise to the dispersion seen in the data in Fig. 4. From this figure, it is apparent that confinement enhancement factors, $\tau^E_{diag}/\tau^E_{ISS04}$, below 1 are attained for reference NBI-heated discharges without PI. In contrast, this factor increases to ∼1.4 for the discharges of interest here. Indeed, a mean value of ∼1.2 is achieved for PI discharges included in Fig. 4.

Now, regarding PiEC reproducibility, the characteristics of the observed PiEC phase in the discharges considered in Fig. 4 are similar to those shown in Fig. 3, albeit with some variation in absolute values. Next, concerning profile reproducibility and plasma density profile evolution along a PiEC phase, the shot-by-shot method using the TS diagnostic with reproducible discharges and pellets is employed. This was done for selected discharges from 52549 to 52561 into which a single pellet with 1.2×10^{19} ($\pm 5 \times 10^{17}$) H atoms was injected, while the TS was fired at different times after PI (see Fig. 5). Indeed, good post-injection density profile reproducibility can be appreciated from this figure. Moreover, it is seen also how, well after pellet injection, the density profiles grow and broaden slightly until NBI switch-off (40 ms after PI in this case). In parallel, temperature profiles remain relatively unchanged, i.e., within error bars. Thus, in conclusion, it can be considered that good PiEC reproducibility is achieved.

B. Performance bifurcation in ISS04 scaling law

In terms of overall plasma performance, a bifurcation can be clearly identified in the pellet-fueled NBI-heated discharges investigated here. Here, a bifurcation is understood to be a significant change (improvement) of confinement properties at unchanged values of the external drive of the system (here: NBI heating), lasting much longer than the initial, transitory effect of density enhancement caused by the pellet itself. This bifurcation can be seen in Fig. 6 in which the triple product, $n_e \cdot T_i \cdot \tau^E$, is plotted using τ^E_{diag} and τ^E_{ISS04} as a function of time for two discharges of the series presented in Fig. 3, i.e., 49742 and 49751. These plots are shaded in order to highlight the different plasma phases that can be identified, i.e., a pre-injection phase, a short pellet ablation and homogenization phase, a post-injection transition phase, a PiEC phase, and a decay phase, the latter occurring after the NBI beam switch-off. Although PIs are made at different times in these discharges, it is seen that, prior to PI, the products $n_e \cdot T_i \cdot \tau^E_{diag}$ and $n_e \cdot T_i \cdot \tau^E_{ISS04}$ are in close agreement, whereas after PI, a clear bifurcation toward higher values appears during the highlighted transition phase. The resultant improved performance continues until plasma NBI heating switch-off. This same behavior can be noted when the triple products are plotted as a function of interferometer line integral density, $\int n_e\, dl$ (see Fig. 6(c)). Here, the error bars in Fig. 6 originate from uncertainties in estimating the τ's since the P_{abs} used to estimate these has a 10%–15% uncertainty, according to the FAFNER2 code.

C. Post-injection plasma characteristics

In order to further understand such a PiEC phase, plasma potential profiles, obtained along discharge 49744 using HIBP#2, are shown in Fig. 7. It should be noted that a HIBP scan between the low-field side (LFS) and high-field side (HFS) edges requires ∼20.5 ms, and thus, the plasma evolves to some degree along a scan period. Nonetheless, it is seen in Fig. 7 that φ, which is negative across scanned radii before PI, becomes more negative after PI inside $\rho = 0.7$ (it is not possible to confirm this tendency inside $\rho = \sim 0.25$ due to reduced HIBP signal levels). In this example, the pre-injection φ values are close to the minimum φ values that have been measured for this 100_44_64 configuration.[42] Next, the local φ, as measured by HIBP#1 when fixed close to $\rho = 0.5$, follows a similar trend, becoming more negative after PI and remaining so until the discharge ends [see Fig. 8(a)]. The HIBP#1 current, I_{HIBP}, in the same figure drops immediately after PI, as the HIBP beam current is attenuated significantly by the post-injection density increase and remains attenuated until the end of the discharge. It is also interesting to compare these HIBP#1 measurements with those at another fixed radial position, i.e., at $\rho = 0.7$. At $\rho = 0.7$, φ measurements [see Fig. 8(b)] show a slight rise to a less negative φ for a brief period after PI, which subsequently becomes more negative. Finally, in terms of fluctuations, significant reductions are observed for I_{HIBP} and φ at $\rho = 0.5$, but not at $\rho = 0.7$. Indeed, the root mean squares (RMSs) of both I_{HIBP} and φ reduce immediately after PI at $\rho = 0.5$, and remain so before increasing slightly at ∼15 ms later, albeit to values lower than pre-PI values.

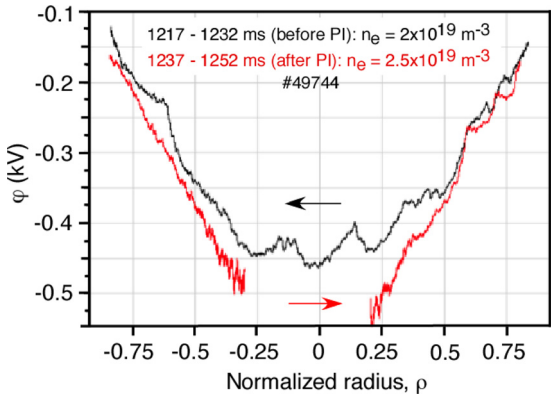

FIG. 7. φ profiles obtained with HIBP#2 before PI (gray, between 1217 and 1232 ms), and after PI (red, 1237–1252 ms). The arrows indicate the scan directions. Some smoothing has been applied here to the signals. Note: data are unavailable inside $\rho = 0.25$ after PI because of I_{HIBP} signal attenuation due to increased plasma density and outside $\rho = \sim 0.75$ due to high signal-to-noise levels. (Figure is courtesy of A. Melnikov, M. Drabinskiy, L. G. Eliseev, and P. Khabanov.)

In another set of discharges, a pellet with 7.5×10^{18} H atoms is injected into plasma created in the magnetic configuration 100_40_63 with $\iota_0/2\pi = 1.51$, but with a lower target $\langle n_e \rangle$, i.e., 1.6×10^{19} m^{-3}, than the plasma considered in Fig. 3. In these discharges, the factor $\tau^E_{diag}/\tau^E_{ISS04}$ increases from 0.77 (without PI) to 1.1 (after PI) at maximum W^E_{diag}. Moreover, tomographic reconstructions of bolometer measurements for these same discharges show how plasma emissivity increases in the plasma core region ($\rho \leq \sim 0.7$) after PI compared to core emissivity in the reference discharge and remains so until NBI heating switch-off. In parallel, emissivity remains low for $\rho \geq \sim 0.7$ for both discharges (see Fig. 9). For these same discharges, the evolution of E_r is followed at two radial positions in the outer region using the two-channel Doppler reflectometer, i.e., at $\rho = 0.75$ and $\rho = 0.82$. See Fig. 10. It is found that E_r becomes more negative immediately after

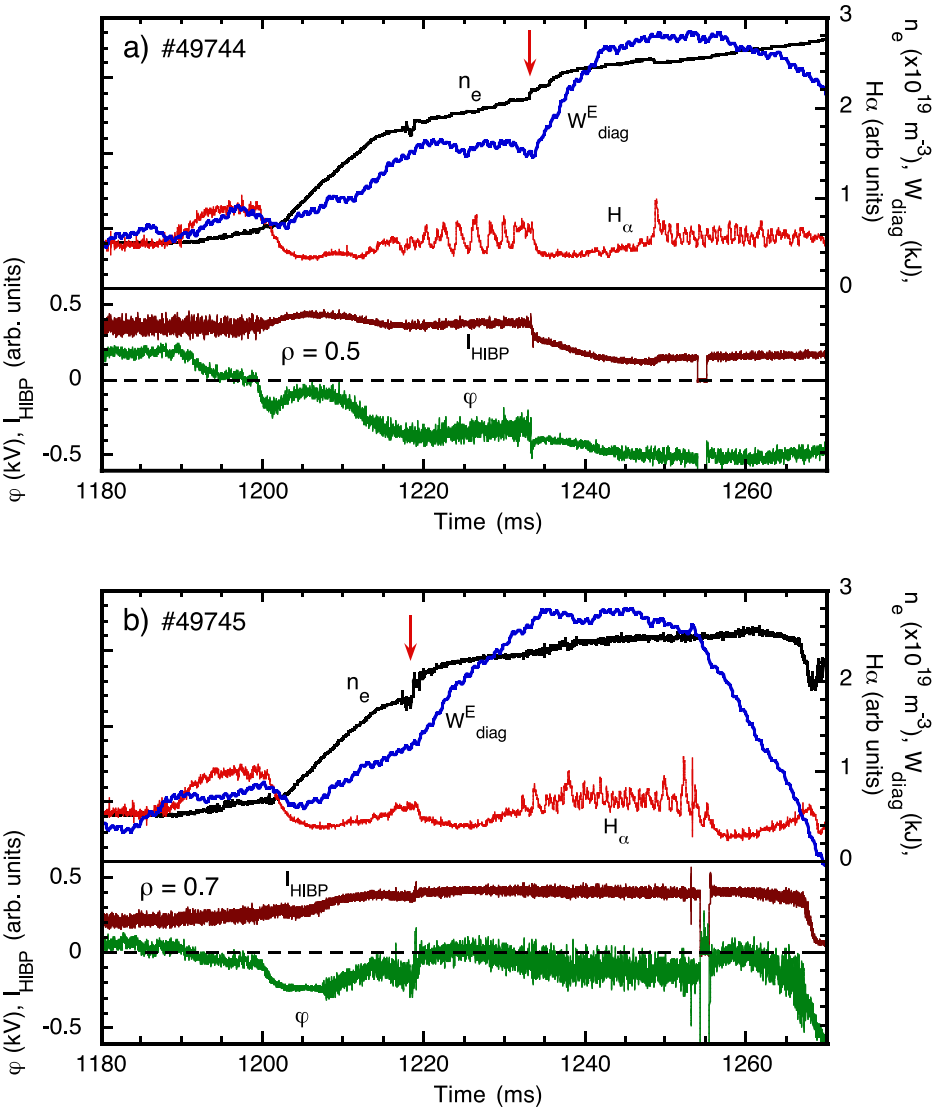

FIG. 8. Evolution of selected plasma parameters along the NBI-heated phase of TJ-II discharges, (a) 49744 and (b) 49745. A pellet is injected at 1233.07 ms (49744) and at 1218.79 ms (49745). *Top*: Hα signal (red), stored diamagnetic energy, W^E_{diag} (blue), and line-averaged electron density, n_e (black). *Bottom*: Evolution of HIBP#1 current, I_{HIBP}, and local plasma potential, φ, at $\rho = 0.5$ (49744) and at $\rho = 0.7$ (49745). Some smoothing has been applied to φ signals. I_{HIBP} is related to local plasma density attenuation along the primary Cs^+ and secondary Cs^{+2} beam paths.

PI, as compared to a discharge without PI, and remains so for the remainder of the discharge. However, for these discharges, electron density fluctuation levels in both channels appear to be unaffected by a pellet injection [see Fig. 10(c)]. Unfortunately, it is not possible to compare absolute Doppler and HIBP E_r values at outer ρ as HIBP signal noise levels increase significantly at these radii.

IV. NEOCLASSICAL AND TRANSPORT CODE SIMULATIONS

Prior to describing NC and transport code simulations, the general plasma characteristics analyzed here are outlined. Figure 11 shows an example of electron density and temperature profiles from a series of discharges with and without a PiEC phase. It should be noted that n_{e0} grows from $\sim 2.5 \times 10^{19}$ m^{-3} to $\sim 4.4 \times 10^{19}$ m^{-3} due to the injection of a pellet containing $\sim 1.5 \times 10^{19}$ H atoms into plasma heated by NBI#1 only. In this case, during the immediate post-injection evolution of the plasma, an increase in n_e is observed together with an abrupt decrease in T_e, this being followed by a recovery of T_e to pre-injection values across the full plasma radius, in similar way that the series shown in Fig. 3. Once this short transitory post-injection phase is over and the enhanced confinement phase is achieved, the most notable post-injection change in n_e and T_e profiles, when compared to pre-injection phase or plasmas without PI, is the sustained increase in core density (Fig. 11) together with enhanced n_e gradients [Fig. 11(c)]. In these discharges, the factor $\tau^E_{diag}/\tau^E_{ISS04}$ increases from 0.89 (without PI) to 1.04 (PiEC) at maximum W^E_{diag}. It should be pointed out also that the sustained increase observed here cannot be accounted for by fueling from the ~32 keV heating beam, which provides 580 kW of port-through power (~410 kW of absorbed power), i.e., $\sim 7.5 \times 10^{19}$ H atoms/s are provided by each beam, which correspond to $\sim 7.5 \times 10^{17}$ H atoms in 10 ms.

Neoclassical (NC) simulations are performed to compare transport properties for NBI-heated plasmas with and without PI and thus obtain some insight into the processes that are acting here.[43–45] In the

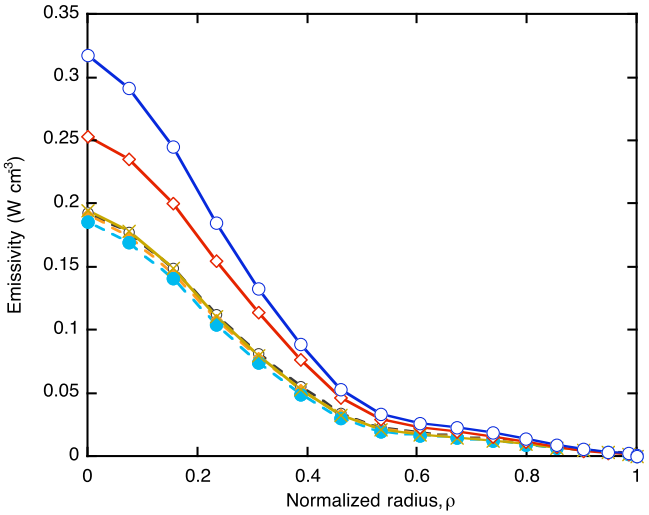

FIG. 9. Plasma emissivity profiles reconstructed from bolometer array signals for several time instances along two TJ-II discharges. Profiles are shown for discharge 43870 (dash) and 43871 (continuous) at 1198 (squares), 1200.5 (diamonds), and 1208 ms (circles). A pellet with 7.5×10^{18} H atoms is injected into 43871 at 1197.89 ms. No pellet is injected into 43870.

simulations made using the profiles shown in Fig. 11, the radial electric field E_r obtained from solving the ambipolar condition shows negative E_r values up to $\rho \sim 0.7$ with a positive gradient for $\rho > 0.5$. The main differences between the PiEC phases compared to the reference NBI-heated phase are a more negative and larger E_r shear. The possible connection between observed reductions in density as well as in plasma potential fluctuations and these predictions requires further study. Here, the local confinement times can be estimated from the ambipolar particle, $\Gamma(r)$, and heat, $Q(r)$, fluxes using a cylindrical approximation, which leads to the ambipolar particle confinement time

$$\tau^p(r) = \frac{4\pi^2 R \int_0^r n(r')r'dr'}{4\pi^2 Rr\Gamma(r)} \quad (1)$$

and energy confinement time

$$\tau^E(r) = \frac{4\pi^2 R \int_0^r \frac{3}{2} n(r')\left[T_e(r') + T_i(r')\right]r'dr'}{4\pi^2 Rr[Q_e(r) + Q_i(r)]}. \quad (2)$$

These two expressions strongly increase toward the plasma axis and edge, i.e., where fluxes are smaller. This is because fluxes are proportional to gradients near the axis, whereas at the edge, there exists a decreasing dependence of diffusion coefficients with collisionality. The common trade-off consists of using the lowest radial values that usually correspond to the position with largest gradients, i.e., around $\rho \sim 2/3$. The result of comparing without and with a PiEC phase shows an increase in the ambipolar particle and heat fluxes, i.e., the denominators in Eqs. (1) and (2), due to higher density and basically the same temperature, see Fig. 11. However, this increase is counteracted by a larger increase in the number of particles and the energy that appear in the numerators, this leading to an improved energy and confinement times.

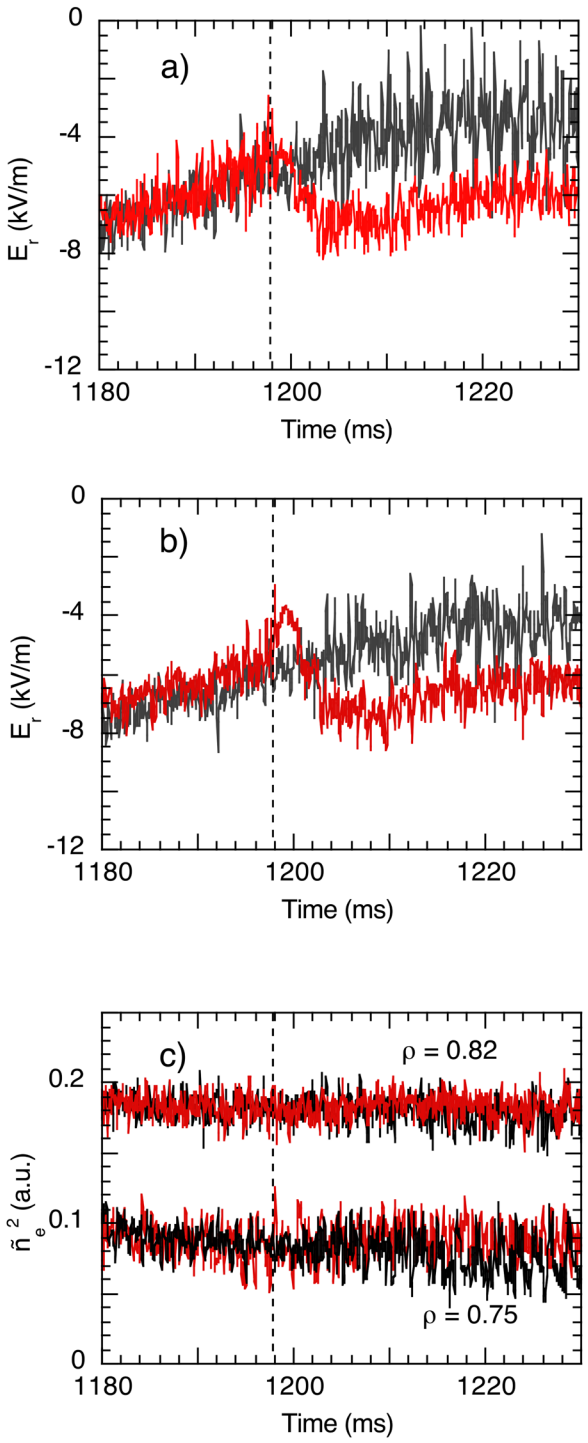

FIG. 10. Temporal evolution along two NBI-heated TJ-II discharges of E_r and density fluctuation levels as measured by the two-channel Doppler reflectometer at different radial positions. The plots show E_r measured (a) at $\rho = 0.75$ and (b) at $\rho = 0.82$ plus (c) the back-scattered power (proportional to $\tilde{n}_e^2$) measured at the same radial positions, for discharges 43870 (gray) and 43871 (red). A pellet with 7.5×10^{18} H atoms is injected into 43871 at 1197.89 ms. No pellets are injected into 43870.

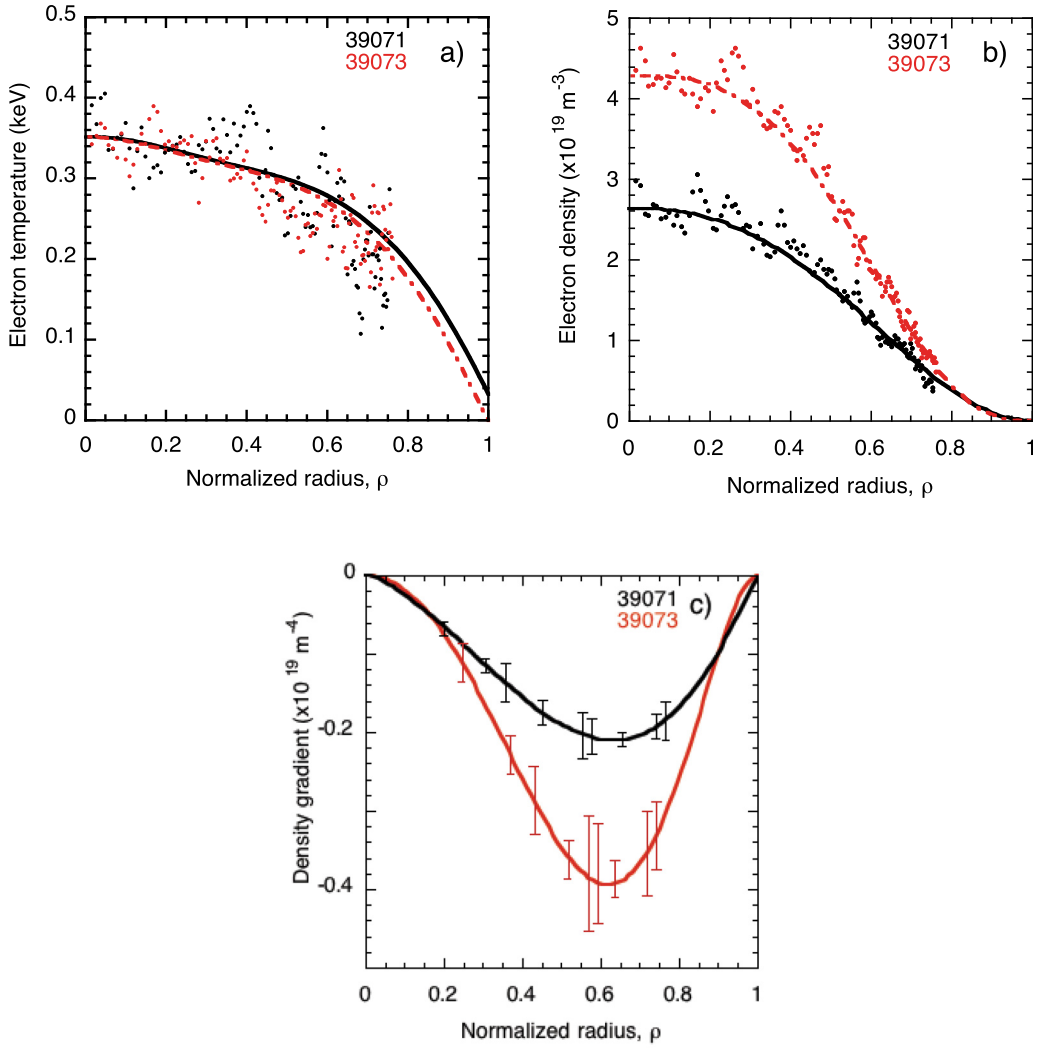

FIG. 11. Electron temperature (a) and density (b) profiles obtained using the Thomson Scattering system for TJ-II discharges 39071 (before PI, continuous black) and 39073 (18.1 ms after a pellet with 1.5×10^{19} H atoms is injected, dash–dot red). Both plasmas are heated by a single NBI (NBI#1) that provides 550 kW of port-through power. (c) Density gradients for the same profiles. The error bars in (c) are estimated from the dispersion in the TS data.

Preliminary predictive modeling was also done, using the ASTRA transport code, for pellet injection into these NBI-heated plasmas in TJ-II.[46,47] These simulations considered particle sources coming from pellet ablation as well as from recycling and heating beam deposition. In addition, the electron source and neutral profiles were obtained from an adaptation of the Eirene code for the TJ-II geometry.[48] Furthermore, the Fafner Monte Carlo code,[49] interleaved with Eirene, was used to update NBI deposition profiles,[39] this allowing

TABLE I. Comparison of experimental energy confinement times, τ^E, with ISS04 scaling law,[23] τ^{ISS04}, and NC simulations[40–42] at $\rho = 2/3$, $\tau^E(\rho = 2/3)$, for the discharges in Fig. 10. Here, PiEC refers to an NBI-heated plasma with a pellet-induced enhanced confinement phase and No-PI refers to reference plasma without pellet injection.

	τ^E	τ^{ISS04}	$\tau^E(\rho = 2/3)$
No-PI	3.2 ms	3.6 ms	9 ms
PiEC	4.9 ms	4.7 ms	13 ms

TABLE II. Comparison of particle confinement times, τ^P, obtained with the NC simulations[43–45] at $\rho = 2/3$ and ASTRA[46–49] for the discharges presented in Fig. 10. Here, PiEC refers to an NBI-heated plasma with a pellet-induced enhanced confinement phase and No-PI refers to reference plasma without pellet injection.

	τ^P $(\rho = 2/3)$	τ^P
No-PI	22 ms	16 ms
PiEC	30 ms	19 ms

calculation of the particle confinement time evolution. Initial simulations show a reduction of the electron thermal diffusivity, χ_e, in the region $\rho \leq 0.7$ several milliseconds after PI. In addition, the particle confinement time increases from ~10 to ~19 ms, while E_r becomes more negative in the region $\rho = 0.5$–0.7.

The experimental values of τ^E are compared with those obtained from the transport simulations and the ISS04 scaling law in Table I with and without PiEC. Although there exists fair agreement between the experimental and ISS04 values, the NC estimation is a factor of 2.5 higher. There are two main factors that may add-up to create this discrepancy. First, the conditions for the application of NC are only marginally applicable to these plasmas, and second, the uncertainties in the ion temperature profile, the Z_{eff}, and the dominant impurity of the plasma (assumed to be carbon). However, in contrast, the qualitative agreement can be considered to be reasonably good. For instance, the boost in experimental energy confinement times between with and without a PiEC phase for these shots is ~50%, whereas the improvements in ISS04 and NC simulations in Table I are 30% and 45%, respectively.

A comparison of the particle confinement times for the ASTRA and NC simulations with and without PI appears in Table II. Although it is not possible to conclude that there is good agreement, in view of the quite different approximations and modeling used and the uncertainties in some of the input parameters, as explained above, the disagreement cannot be classified as bad. In addition, again, there is a fair qualitative agreement between the cases with and without PI.

V. DISCUSSIONS AND SUMMARY

A pellet-induced enhanced confinement regime that lasts for more than two particle confinement times after PI has been observed for the first time in NBI-heated plasmas of the stellarator TJ-II. When experimental energy confinement times are compared with values predicted using the ISS04 Scaling law, an improvement of up to 40% is observed for post-injection line-averaged electron densities between 2.5 and 3.5 $\times$ 10^{19} m^{-3}. As noted in the text, while pre- and post-injection T_e profiles and T_{i0} are similar, a significant rise occurs in core n_e after PI, i.e., inside $\rho = \sim 0.7$. The result is a bifurcation in plasma performance in which the triple product, $n_e \cdot T_i \cdot \tau^E$, achieves values that are significantly higher than those obtained by other plasma fueling methods. Indeed, in TJ-II, these higher values are maintained until NBI heating is switched-off. In comparison, in the W7-X, a transient high-performance phase was also observed after multi-pellet injection into some discharges.[3] It was reported therein that the plasma moves to a different branch of $n_e \cdot T_i \cdot t^E$ after a train of PIs, this being followed by a return to normal confinement as the plasma density decayed. It was considered that the existence of two such branches, as reported here for TJ-II, indicates a "performance bifurcation" in these devices.[50] It is also helpful to consider here the evolution of plasma beta, β. For instance, plasma central beta, β_0, increases significantly during a PiEC phase, i.e., from 0.38% to 0.65% for the example considered in Fig. 10, while β rises by ~35%, i.e., from ~0.22% to ~0.3%. In contrast, the stability/equilibrium β limit for the configuration 100_44_64 is predicted to be ~3%.[51] However, closer agreement is attained if the β limit deduced from Sudo's scaling, $\beta^S(\%) = 0.55\ P_{abs}^{0.77}\ B^{-0.82}\ a^{-0.69}\ R^{-0.6} = \sim 0.6\%$,[11] is used for comparison with experimental β's. In either case, these discharges are not terminated by radiation collapse; thus, higher β values should be achievable if additional pellet material can be deposited in the core. Thus, it is proposed to undertake new experiments involving a train of pellet injections closely spaced in time in order to investigate these limits in TJ-II.

As noted previously, the main experimental observation along a PiEC phase is the increased core density after a PI and similar pre- and post-injection T_e and T_i values. The latter could indicate that temperature profiles play a minor role in PiEC maintenance; however, it is not clear if temperature profiles play a role in PiEC formation. In contrast, the density gradient becomes significantly steeper, in particular in the region about $\rho = \sim 0.6$. Indeed, the neoclassical simulations presented here predict large changes in E_r across a broad radial range, with the largest changes occurring close to $\rho = \sim 0.6$. Moreover, predicted ambipolar particle and heat fluxes also support improvements in particle and energy confinement times, this being not inconsistent with values derived from the ISS04 scaling law, i.e., $\tau^E_{diag}/\tau^E_{ISS04} = 1.2$ for the data presented in Fig. 4 and $\tau^E_{diag}/\tau^E_{ISS04} = 1.4$ for the discharges examined in detail in Sec. III. Unfortunately, measured and estimated E_r's cannot be compared here for the plasma core as it has proved challenging to follow PI-induced changes in E_r using a HIBP as its profile scan time is relatively long and signal levels decrease when plasma density rises. Nonetheless, there are indications that plasma potential becomes more negative in the core after PI and that E_r is tending to become more negative inside $\rho = 0.7$. Indeed, measurements of E_r at $\rho = 0.75$ and $\rho = 0.82$ using a Doppler reflectometer reveal more negative E_r values in the edge region after a PI. In contrast, density and φ fluctuation levels appear to be unaffected by PI in the edge region, whereas reductions are observed in such fluctuations at inner radii, i.e., at $\rho = 0.5$, when using a HIBP. Finally, as outlined in Sec. III B, radiation losses show increased peaking in the plasma core during a PiEC phase, while such losses remain low in the edge region.

In summary, we compare PiEC and reference plasma characteristics in NBI-heated scenarios in the stellarator TJ-II. After an analysis of experimental data, a clear increase in energy confinement time is observed once ablated pellet material has been homogenized about the plasma. Moreover, the heating NBI is capable of maintaining this improved performance phase (PiEC) until beam switch-off. In addition, a bifurcation is identified in the plasma triple product diagram, where a 40% increase in performance is found when the experimental and ISS04 scaling branches are compared. Furthermore, a strong increase in plasma density gradient is observed in the region $\rho = \sim 0.6$, together with a clear reduction of density and potential fluctuations in the same region. While not enabling identification of a mechanism for such an improved performance, NC calculations predict more negative E_r and increased τ^E, which agree qualitatively, but not quantitatively, with experimental tendencies. However, the contribution of turbulence to these observations still needs to be quantified; thus, investigation of a mechanism that leads to the observed improvements is still under investigation. In comparison, in the W7-X, a transient increase in energy confinement time was observed after PIs.[3] While, in the W7-X, the stabilization of ion temperature gradient (ITG) modes seems to be a key player in the observed enhanced confinement, ITG modes are not the dominant instabilities for turbulent transport in the TJ-II. Finally, the identification of the mechanism for enabling this enhanced confinement phase in TJ-II is still subject to ongoing investigation.

ACKNOWLEDGMENTS

This work is financed by grants PID2020-116599RB-I00 and PID2021-125607NB-I00, funded by MCIN/AEI/10.13039/501100011033. This work has been carried out within the framework of the EUROfusion Consortium, funded by the European Union via the Euratom Research and Training Programme (Grant Agreement No. 101052200 - EUROfusion). Views and opinions expressed are those of the author(s) only and do not necessarily reflect those of the European Union or the European Commission. Neither the European Union nor the European Commission can be held responsible for them. The authors acknowledge the contributions to HIBP data collection, analysis, and interpretation made by A. Melnikov, M. Drabinskiy, L. G. Eliseev, and P. Khabanov as part of the long-term trilateral collaboration between National Research Center 'Kurchatov Institute,' Moscow, Russia, led by S. Melnikov, the HIBP group from Kharkov Institute of Physics and Technology, Kharkov, Ukraine, leaded by L.I. Krupnik, and CIEMAT. We also acknowledge the TJ-II Team.

AUTHOR DECLARATIONS

Conflict of Interest

The authors have no conflicts to disclose.

Author Contributions

Isabel García Cortés: Conceptualization (equal); Data curation (equal); Formal analysis (equal); Funding acquisition (equal); Investigation (equal); Methodology (equal); Project administration (equal); Resources (equal); Software (equal); Supervision (lead); Validation (equal); Visualization (equal); Writing – original draft (lead); Writing – review & editing (lead). **Raul Garcia:** Software (equal). **Julio Hernández-Sánchez:** Software (equal). **Carlos Hidalgo:** Data curation (equal). **A. S. Kozachek:** Data curation (equal). **FRANCISCO MEDINA:** Data curation (equal). **Maria Antonia Ochando:** Data curation (equal). **Jose Luis de Pablos:** Data curation (equal). **Nerea Panadero:** Data curation (equal). **Ignacio Pastor:** Data curation (equal). **Kieran Joseph McCarthy:** Conceptualization (equal); Data curation (equal); Formal analysis (equal); Funding acquisition (equal); Investigation (equal); Methodology (equal); Project administration (equal); Resources (equal); Software (equal); Supervision (equal); Validation (equal); Visualization (equal); Writing – original draft (equal); Writing – review & editing (equal). **Teresa Estrada:** Data curation (equal); Methodology (equal). **Victor Tribaldos:** Data curation (equal). **Daniel Medina-Roque:** Data curation (equal); Methodology (equal). **Boudewijn Philip van Milligen:** Visualization (equal). **Enrique Ascasibar:** Data curation (equal). **Ricardo Carrasco:** Resources (equal). **A. Chmyga:** Data curation (equal).

DATA AVAILABILITY

The data that support the findings of this study are available from the corresponding author upon reasonable request.

REFERENCES

[1]M. Greenwald, D. Gwinn, S. Milora, J. Parker, R. Parker, S. Wolfe, M. Besen, F. Camacho, S. Fairfax, C. Fiore *et al.*, Phys. Rev. Lett. **53**, 352 (1984).
[2]L. R. Baylor, P. B. Parks, T. C. Jernigan, J. B. Caughman, S. K. Combs, C. R. Foust, W. A. Houldberg, S. Maruyama, and D. A. Rasmussen, Nucl. Fusion **47**, 443 (2007).
[3]J. Baldzuhn, H. Damm, C. D. Beidler, K. McCarthy, N. Panadero, C. Biedermann, S. A. Bozhenkov, A. Dinklage, K. J. Brunner, G. Fuchert *et al.*, Plasma Phys. Controlled Fusion **62**, 055012 (2020).
[4]P. T. Lang, T. C. Blanken, M. Dunne, R. M. McDermott, E. Wolfrum, V. Bobkov, F. Felici, R. Fischer, F. Janky, A. Kallenbach *et al.*, Nucl. Fusion **58**, 036001 (2018).
[5]N. Ohyabu, T. Morisaki, S. Masuzaki, R. Sakamoto, M. Kobayashi, J. Miyazawa, M. Shoji, A. Komori, O. Motojima, and LHD Experimental Group, Phys. Rev. Lett. **97**, 055002 (2006).
[6]R. Sakamoto, H. Yamada, K. Tanaka, K. Narihara, S. Morita, S. Sakakibara, S. Masuzaki, S. Inagaki, L. R. Baylor, P. W. Fisher *et al.*, Nucl. Fusion **41**, 381 (2001).
[7]G. Motojima, H. Okada, H. Okazaki, S. Kobayashi, K. Nagasaki, R. Sakamoto, H. Yamada, S. Kado, S. Ohshima, T. Minami *et al.*, Plasma Phys. Controlled Fusion **61**, 075014 (2019).
[8]A. A. Belokurov, L. G. Askinazi, L. Chôné, E. Z. Gusakov, T. P. Kiviniemi, V. A. Kornev, T. Korpilo, S. V. Krikunov, S. V. Lebedev, S. Leerink *et al.*, Nucl. Fusion **58**, 112007 (2018).
[9]M. Valovič, L. Garzotti, C. Gurl, R. Akers, J. Harrison, C. Michael, G. Naylor, R. Scannell, and MAST Team, Nucl. Fusion **52**, 114022 (2012).
[10]K. J. McCarthy, N. Panadero, J. L. Velasco, S. K. Combs, J. B. O. Caughman, J. M. Fontdecaba, C. Foust, R. García, J. Hernández Sánchez, M. Navarro *et al.*, Nucl. Fusion **57**, 056039 (2017).
[11]S. Sudo, Y. Takeiri, H. Zushi, F. Sano, K. Itoh, K. Kondo, and A. Hyoshi, Nucl. Fusion **30**, 11 (1990).
[12]A. Dinklage, R. Sakamoto, M. Yokoyama, K. Ida, J. Baldzuhn, C. D. Beidler, S. Cats, K. J. Mc Carthy, J. Geiger, M. Kobayashi *et al.*, Nucl. Fusion **57**, 066016 (2017).
[13]O. Kaneko, M. Yokoyama, M. Yoshinuma, K. Nagaoka, K. Ida, R. Sakamoto, T. Akiyama, N. Askikawa, H. Chikaraishi, M. Emoto *et al.*, Plasma Fusion Res. **4**, 27 (2009).
[14]K. Ida, K. Kondo, K. Nagasaki, T. Hamada, S. Hidekuma, F. Sano, H. Zushi, T. Mizuuchi, H. Okada, S. Besshou *et al.*, Plasma Phys. Controlled Fusion **38**, 1433 (1996).
[15]C. D. Beidler, H. M. Smith, A. Alonso, T. Andreeva, J. Baldzuhn, M. N. A. Beurskens, M. Borchardt, S. A. Bozhenkov, K. J. Brunner, H. Damm *et al.*, Nature **596**, 221 (2021).
[16]S. A. Bozhenkov, Y. Kazakov, O. P. Ford, M. N. A. Beurskens, J. Alcusón, J. A. Alonso, J. Baldzuhn, C. Brandt, K. J. Brunner, and H. Bamm, Nucl. Fusion **60**, 066011 (2020).
[17]T. Estrada, D. Carralero, T. Windisch, E. Sánchez, J. M. García-Regaña, J. Martínez-Fernández, A. de la Peña, J. L. Velasco, J. A. Alonso, M. Beurskens *et al.*, Nucl. Fusion **61**, 046008 (2021).
[18]K. J. McCarthy, N. Tamura, S. K. Combs, N. Panadero, E. Ascasíbar, T. Estrada, R. García, J. Hernández Sánchez, A. López Fraguas, M. Navarro *et al.*, Europhys. Lett. **120**, 25001 (2017).
[19]N. Panadero, K. J. McCarthy, F. Koechl, J. Baldzuhn, J. L. Velasco, S. K. Combs, E. de la Cal, R. García, J. Hernández Sánchez, D. Silvagni *et al.*, Nucl. Fusion **58**, 026025 (2018).
[20]K. J. McCarthy, N. Panadero, S. K. Combs, N. Tamura, E. Ascasíbar, M. Calvo, A. Chmyga, T. Estrada, J. M. Fontdecaba, R. García *et al.*, Plasma Phys. Controlled Fusion **61**, 014013 (2019).
[21]K. J. McCarthy, E. Ascasíbar, N. Tamura, N. Panadero, I. García-Cortés, B. van Milligen, A. Cappa, R. García, J. Hernández-Sánchez, M. Liniers *et al.*, Nucl. Fusion **61**, 076014 (2021).
[22]J. L. Velasco, K. J. McCarthy, N. Panadero, S. Satake, D. López-Bruna, A. Alonso, I. Calvo, A. Dinklage, T. Estrada, J. M. Fontdecaba *et al.*, Plasma Phys. Controlled Fusion **58**, 084004 (2016).
[23]H. Yamada, J. H. Harris, A. Dinklage, E. Ascasíbar, F. Sano, S. Okamura, J. Talmadge, U. Stroth, A. Kus, S. Murakami *et al.*, Nucl. Fusion **45**, 1684 (2005).
[24]E. Ascasíbar, D. Alba, D. Alegre, A. Alonso, J. Alonso, F. de Aragón, A. Baciero, J. M. Barcala, E. Blanco, J. Botija *et al.*, Nucl. Fusion **59**, 112019 (2019).
[25]M. Liniers, G. Wolfers, J. A. Sebastián, B. Rojo, F. Martín, R. Carrasco, J. Guasp, F. Martín, E. Sánchez, A. Jiménez, G. Merino *et al.*, Fusion Eng. Des. **88**, 960 (2013).

[26]F. L. Tabarés, M. Ochando, D. Tafalla, F. Medina, K. McCarthy, J. M. Fontdecaba, M. Liniers, J. Guasp, E. Ascasíbar, T. Estrada *et al.*, Contrib. Plasma Phys. **50**, 610 (2010).
[27]S. K. Combs, C. R. Foust, J. M. McGill, J. B. O. Caughman, K. J. McCarthy, L. R. Baylor, M. Chamorro, D. T. Fehling, R. Garcia, J. H. Harris *et al.*, Fusion Sci. Technol. **64**, 513 (2013).
[28]K. J. McCarthy and TJ-II Team, J. Instrum. **16**, C12026 (2021).
[29]J. Herranz, F. Castejón, I. Pastor, and K. J. McCarthy, Fusion Eng. Des. **65**, 525 (2003).
[30]R. Jiménez-Gómez, A. Könies, E. Ascasíbar, F. Castejón, T. Estrada, L. G. Eliseev, A. V. Melnikov, J. A. Jiménez, D. G. Pretty, D. Jiménez-Rey *et al.*, Nucl. Fusion **51**, 033001 (2011).
[31]F. Medina, L. Rodríguez-Rodrigo, J. Encabo-Fernández, A. López-Sánchez, P. Rodríguez, and C. Rueda, Rev. Sci. Instrum. **70**, 642 (1999).
[32]M. A. Ochando, F. Medina, B. Zurro, A. Baciero, K. J. McCarthy, M. A. Pedrosa, C. Hidalgo, E. Sánchez, J. Vega, A. B. Portas *et al.*, Fusion Sci. Technol. **50**, 313 (2006).
[33]D. Baião, F. Medina, M. Ochando, K. McCarthy, F. Tabarés, I. Pastor, and C. Varandas, Rev. Sci. Instrum. **83**, 053501 (2012).
[34]T. Happel, T. Estrada, E. Blanco, V. Tribaldos, A. Cappa, and A. Bustos, Rev. Sci. Instrum. **80**, 073502 (2009).
[35]A. V. Melnikov, J. M. Barcala, L. I. Krupnik, C. Hidalgo, L. G. Eliseev, A. A. Chmyga, J. Chercoles, A. D. Komarov, A. S. Kozachek, S. M. Knrebtov *et al.*, Fusion Eng. Des. **96–97**, 724 (2015).
[36]A. V. Melnikov, L. I. Krupnik, L. G. Eliseev, J. M. Barcala, A. Bravo, A. A. Chmyga, G. N. Deshko, M. A. Drabinskij, C. Hidalgo, P. O. Khabanov *et al.*, Nucl. Fusion **57**, 072004 (2017).
[37]A. V. Melnikov, L. G. Eliseev, T. Estrada, E. Ascasibar, A. Alonso, A. A. Chmyga, C. Hidalgo, A. D. Komarov, A. S. Kozachek, L. I. Krupnik *et al.*, Nucl. Fusion **53**, 092002 (2013).
[38]J. Guasp, M. Liniers, C. Fuentes, and G. Barrera, Fusion Sci. Technol. **35**, 32 (1999).
[39]J. Guasp, C. Fuentes, and M. Liniers, *Cálculos de inyección de haces neutros para las descargas de TJ-II* (Informes Técnicos Ciemat 1050, Ciemat., Madrid, 2004) (in Spanish).
[40]M. Liniers, J. A. Quintana, B. Rojo, F. Martín-Díaz, F. Miguel, J. A. Sebastián, R. Carrasco, A. Soleto, E. Sánchez-Sarabia, A. Jiménez-Denche *et al.*, J. Instrum. **14**, C09028 (2019).
[41]M. A. Ochando, E. Ascasíbar, A. Baciero, F. Castejón, D. López-Bruna, J. M. Fontdecaba, M. Liniers, K. J. McCarthy, F. Medina, I. Pastor *et al.*, in *Proceedings of the 41st EPS Conference on Plasma Physics* (European Physical Society, 2014), p. P2.074.
[42]A. V. Melnikov, A. Alonso, E. Ascasíbar, R. Balbin, A. A. Chmyga, Y. N. Dnestrovskij, L. G. Eliseev, T. Estrada, J. M. Fontdecaba, C. Fuentes *et al.*, Fusion Sci. Technol. **51**, 31 (2007).
[43]V. Tribaldos, Phys. Plasmas **8**, 1229 (2001).
[44]V. Tribaldos, C. D. Beidler, Y. Turkin, and H. Maassberg, Phys. Plasmas **18**, 102507 (2011).
[45]Y. Turkin, C. D. Beidler, H. Maassberg, S. Murakami, V. Tribaldos, and A. Wakasa, Phys. Plasmas **18**, 022505 (2011).
[46]D. López-Bruna, J. M. Reynolds, A. Cappa, J. Matínez, J. García, and C. Gutierrez-Tapia, see documenta.ciemat.es/bitstream/123456789/114/1/40921_IC1201.pdf for "Informes Técnicos Ciemat 1201, Ciemat. Madrid, 2010," (in Spanish).
[47]I. Arapoglou, see www-fusion.ciemat.es/MasterThesis/Arapoglou.pdf for "A hydrogen pellet injector for the TJ-II stellarator: Testing, modelling and first experiments," 2014.
[48]J. Guasp and A. Salas, see eirene.de/html/relevant_reports.html for "Eirene user manual for Ciemat," 2006.
[49]A. Teubel and F. P. Penningsfeld, Plasma Phys. Controlled Fusion **36**, 143 (1994).
[50]A. Dinklage, private communication (2022).
[51]A. Varias, C. Alejandre, A. L. Fraguas, L. García, B. A. Carreras, N. Dominguez, and V. E. Lynch, Nucl. Fusion **30**, 2597 (1990).